An improved dynamic bidirectional coupled hydrologic-hydrodynamic model for efficient flood inundation prediction

Yanxia Shen, Zhenduo Zhu, Qi Zhou, Chunbo Jiang[*]

State Key Laboratory of Hydroscience and Engineering, Department of Hydraulic

Engineering, Tsinghua University, Beijing, 100084, China

Abstract: To improve computational efficiency while maintaining numerical accuracy, coupled hydrologic-hydrodynamic models based on non-uniform grids are used for flood inundation prediction. In those models, a hydrodynamic model using a fine grid can be applied for flood-prone areas, and a hydrologic model using a coarse grid can be used for the remaining areas. However, it is challenging to deal with the separation and interface between the two types of areas because the boundaries of the flood-prone areas are time-dependent. We present an improved Multigrid Dynamical Bidirectional Coupled hydrologic-hydrodynamic Model (IM-DBCM) with two major improvements: 1) automated non-uniform mesh generation based on the $D\infty$ algorithm was implemented to identify the flood-prone areas where high-resolution inundation conditions are needed; 2) ghost cells and bilinear interpolation were implemented to improve numerical accuracy in interpolating variables between the coarse and fine grids. A hydrologic model, two-dimensional (2D) nonlinear reservoir model was bidirectionally coupled with a 2D hydrodynamic model that solves the shallow water equations. Three cases were considered to demonstrate the effectiveness of the improvements. In all cases, the mesh generation algorithm was shown to efficiently and successfully generate high-resolution grids in those flood-prone areas. Compared with the original M-DBCM (OM-DBCM), the new model had lower RMSEs and higher

---

[*]Corresponding author: State Key Laboratory of Hydroscience and Engineering, Department of Hydraulic Engineering, Tsinghua University, Beijing, 100084, China
Corresponding author: Tel: +8613581891886; E-mail address: jcb@tsinghua.edu.cn

24 NSEs, indicating that the proposed mesh generation and interpolation were reliable and

25 stable. It can be adapted adequately to the real-life real flood evolution process in

26 watersheds and provide practical and reliable solutions for rapid flood prediction.

27 **Key words:** Coupled hydrologic-hydrodynamic model; Multi-grid generation; Bilinear

28 interpolation; Computational efficiency and accuracy; Flood simulation

29 **1 Introduction**

30   Floods are the most frequent natural disasters that seriously harm human health

31 and economic growth. Numerical models are critical for predicting flooding processes

32 to help prevent or mitigate the damaging effects of floods on people and communities

33 (Bates, 2022). Coupled hydrologic-hydrodynamic models are widely used to translate

34 the amount of rainfall obtained from weather forecasting models or rain gauge

35 observations into surface inundation (Xia et al., 2019).

36   Coupled hydrologic-hydrodynamic models can be generally divided into external

37 (one-way) and internal (two-way) coupling models (see Figure 1). The external

38 coupling models utilize hydrographs obtained from hydrologic models as an input for

39 hydrodynamic models in a fixed position, providing a one-way transition (Schumann

40 et al., 2013; Feistl et al., 2014; Choi and Mantilla, 2015; Bhola, 2018; Wing et al., 2019).

41 It is powerful tools for watershed flood simulation, in particular large spatial and

42 temporal scale, due to its convenience in model construction. However, this one-way

43 flow information cannot capture the mutual interaction between runoff production and

44 flood inundation, and the fixed interface is inconsistent with the actual flood process

45 where the inflow discharge positions, flow path, and discharge values change with

46 accumulating rainfall.
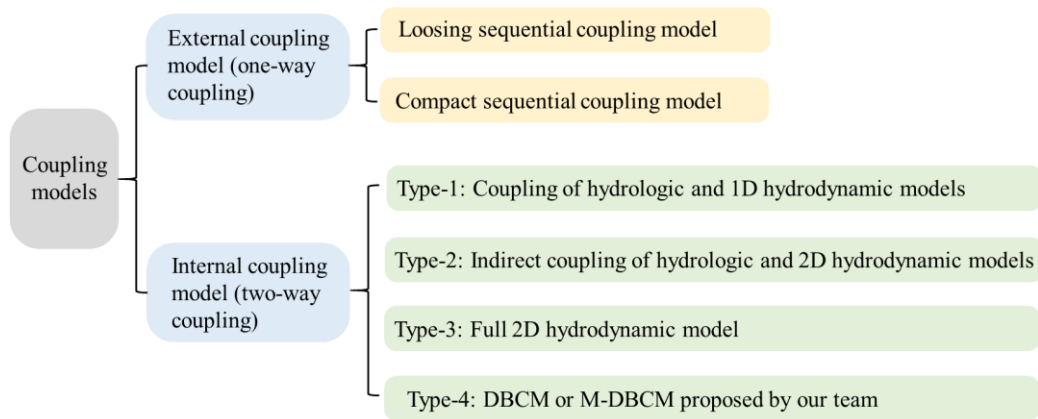
Figure 1 Classifications of coupled hydrologic and hydrodynamic models

The two-way coupling models are further divided into: the coupled hydrologic-1D hydrodynamic model (HH1D), indirect coupled hydrologic-2D hydrodynamic models (ICM2D), full 2D hydrodynamic models (HM2D), and dynamic bidirectional coupling model (DBCM or M-DBCM) proposed by author's team. In the HH1D, the discharges obtained from the hydrologic model is treated as mass source of the 1D hydrodynamic model, while the water depth calculated in 1D hydrodynamic model is fed back to hydrologic model, such as the coupled Mike SHE and Mike 11 (Thompson et al., 2004). The application of 1D modeling of overland flow is limited when developing precise and reliable flood maps in 2D inundation regions.

In order to overcome the lack of 2D hydrodynamic simulation in HH1D, the ICM2D is proposed, where the runoff first flows into 1D rivers, and then discharge into the 2D inundation regions (Seyoum et al., 2012; Chen et al., 2017 and 2018). For example, Mike SHE and Mike11 are coupled to form Mike Urban, and Mike11 and Mike21 are dynamically coupled to form Mike Flood. The indirect coupling between the hydrologic and the 2D hydrodynamic models can be developed by coupling Mike Urban and Mike Flood. The 1D hydrodynamic model is a connection channel between the hydrologic and the 2D hydrodynamic models. Compared with the HH1D, this coupling type has satisfactory and acceptable accuracy and is widely used. As the 2D

67 hydrodynamic model is only calculated in local inundation regions, its computational

68 efficiency is greatly improved in comparison with the HM2D. However, the ICM2D

69 assumed that the water first discharges into the 1D rivers, and then flows from 1D rivers

70 to the 2D regions. The hydrologic model is not directly coupled with the 2D

71 hydrodynamic model, which is inconsistent with the actual flood processes. In reality,

72 water may be discharged into both 1D channel and 2D waterbodies simultaneously, and

73 the hydrologic and 2D hydrodynamic models should be linked directly. Direct coupling

74 of hydrologic and 2D hydrodynamic models can physically reflect the flood processes,

75 which deserves more attention.

76　　In HM2D, the 2D hydrodynamic model is used to simulate the overland flow

77 (runoff routing and flood inundation), and the runoff generation serves as its mass

78 source term (Singh et al., 2011; Garcia-Navarro et al., 2019; Hou et al., 2020; Costabile

79 and Costanzo, 2021). It has satisfactory and acceptable numerical accuracy and has

80 been widely used. But the development and simulation of HM2D require high-

81 resolution topographic data at the catchment scale and extensive computational time,

82 which hinder their application in large-scale flood forecasting (Kim et al., 2012). In

83 HEC-RAS (US Army Corps of Engineers, 2023), for instance, the flooding process in

84 1D rivers was simulated by a 1D hydrodynamic model, whereas the flooding process

85 in 2D regions was simulated using 2D diffusion wave equations (DWEs) or shallow

86 water equations (SWEs). If the 2D regions were discretized into finer grids and the 2D

87 SWEs was applied, the 1D hydrodynamic model was coupled with the 2D SWEs. It has

88 high numerical accuracy but is computationally prohibitive for large-scale applications.

89 Conversely, if the 2D regions were discretized into coarse grids and the 2D DWEs was

90 applied, the 1D hydrodynamic model was coupled with the 2D DWEs, which can

91 expand the application scale at the cost of reducing the accuracy.

Jiang et al. (2021) proposed a DBCM based on uniform structured grids, where the hydrologic and 2D hydrodynamic models were coupled in a two-way manner and the coupling interface of these two models was time-dependent. The model can automatically evolve the surface flow and fully consider the flow states with both mass and momentum transfer. However, because uniform grids were adopted in DBCM, it inevitably increased the computational cost and time, especially in the large watershed.

An essential consideration to reduce computational time is mesh coarsening (Caviedes-Voullième et al., 2012). Adaptive mesh refinement (AMR) has been used to optimize the grid resolution during flood simulations (Donat et al., 2014; Hu et al., 2018; Ghazizadeh, 2020; Ding et al., 2021; Kesserwani and Sharifian, 2023). Aiming to increase computational efficiency by reducing computing nodes, it adjusts grid size for local grid refinement by domain features or flow conditions. Yu (2019) used quadtree grids to divide the computational domain and applied the DBCM to simulate the flooding process. It needs to segment and merge the grid elements repeatedly during the calculation, which can be time-consuming and offset the calculation time saved by the optimized grid. AMR is commonly employed in scenarios where flow characteristics exhibit abrupt variations, such as aerodynamic shock waves, hydraulic jumps, and seismic tsunami waves. Capturing discontinuous solutions necessitates local grid refinement, with the location of refinement dynamically adapting to the position of the discontinuities. AMR is indispensable for this purpose. Flow characteristic variations arising from abrupt geometric changes in the computational domain can be captured using static local refinement grids, provided that the extent of these changes is limited. This approach offers computational time savings.

Static non-uniform grids simplified grid generation procedure compared with AMR (Caviedes-Voullième et al., 2012; Hou et al., 2018; Bomers et al., 2019; Ozgen-

117 Xian et al., 2020). Compared with uniform grids and AMR, it can not only reduce

118 computational nodes, but use different time steps in different grid sizes to further reduce

119 computation time. Shen et al. (2021) and Shen and Jiang (2023) divided the

120 computational domain based on static multi-grids, where the different grid size ratios

121 of coarse to fine grids were designed. But there were two limitations to this scheme.

122 One limitation is that the grids need to be generated manually, which can be subjective

123 and uncertain. It also needs a heavy workload, especially for large watersheds. Besides

124 the grid generation, the variable interpolation between the coarse and fine cells was also

125 not reasonable. There are shared and hanging nodes at the interpolation interface. Shen

126 et al. (2021) assumed the variables at the shared nodes were equal to that at the cell

127 center, and the hanging nodes were calculated by the shared nodes. The results showed

128 that this scheme has unsatisfactory accuracy and frequently fails to converge. Although

129 the multi-grid-based model can reduce computational time, there are remarkable

130 challenges such as the grid partition technique, determination of coarse and fine regions,

131 and variables interpolation between coarse and fine grids.

132 The objective of this study is to develop an integrated system that fully couples

133 the hydrologic and 2D hydrodynamic models, utilize an automated method for efficient

134 multi-grid mesh generation, and resolve variable interpolation between coarse and fine

135 grids more accurately. An improved dynamic bidirectional coupling model (IM-DBCM)

136 was presented, where the 2D nonlinear reservoir (NLR) model was coupled with the

137 2D hydrodynamic model through a CMI. The D∞ algorithm was implemented to divide

138 the computational domain into non-uniform grids automatically. Ghost cells (i.e., the

139 virtual cells located on the boundaries of the computational domain) and bilinear

140 interpolation were used to interpolate variables between the coarse and fine grids. Three

141 case studies were conducted, and the simulation results were compared with the original

142　M-DBCM (OM-DBCM) to evaluate the effectiveness of the improvements.

143　**2 Methodology**

144　　　The Fortran programming language was adopted to apply the coupling model. The

145　framework of IM-DBCM is illustrated in Figure 1. The model consists of two

146　components: a hydrologic model (i.e., 2D NLR) that simulates the runoff generation

147　and routing, and 2D hydrodynamic model simulating the flood inundation process.

148　Before the model setup, it is required to first design the grids. Static multi-grids were

149　applied to the model. For the model execution, the variables interpolation between

150　coarse and fine grids and the coupling of hydrologic and hydrodynamic models are the

151　two main issues that must be addressed.
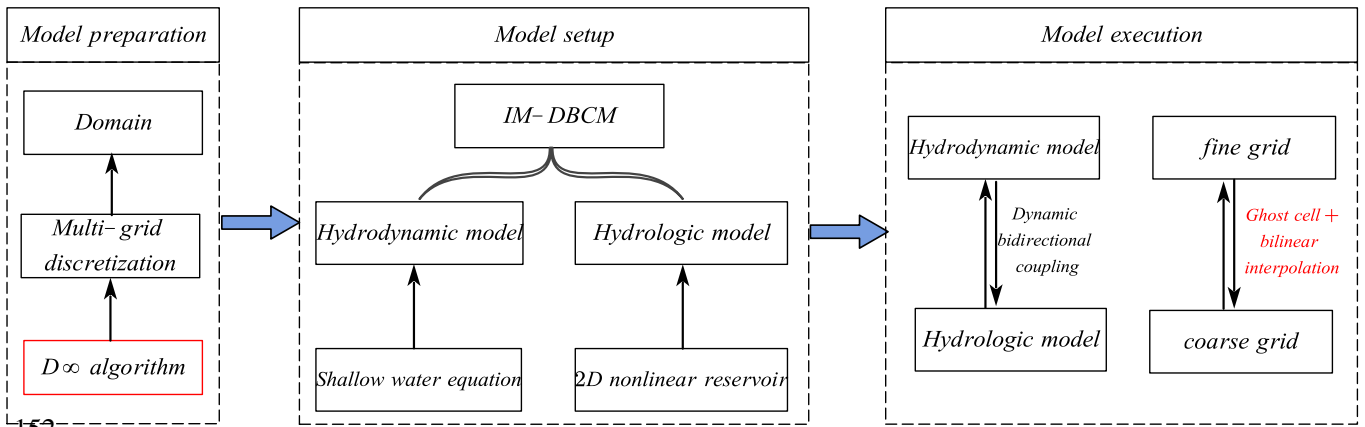
152

153　　　　　　　　　　　　　　　Figure 1 Framework of IM-DBCM

154　**2.1 Automated multi-grid generation**

155　　　Associated with flood models, the design of computational grids that are scalable

156　and suitable for all applications is challenging. The grid generation can be considered

157　as a model preprocess, which is the foundation of flood simulation and can influence

158　both computational accuracy and efficiency. In this study, a multi-grid generation

159　method was proposed based on the D∞ algorithm, to generate refined grid cells at flood-

160　prone areas where high-resolution representation of topographic features is essential for

161　flood simulation while discretizing the rest of the domain using coarse grids. The D∞

7

162   algorithm is a method of representing flow directions based on triangular facets in grid

163   DEM proposed by Tarboton (1997). It allocates the flow fractionally to each lower

164   neighboring grid in proportion to the slope toward that grid. The flow direction is

165   determined as the direction of the steepest downward slope on the eight triangular facets

166   formed across a 3×3-pixel window centered on the pixel of interest, which was detailed

167   by Tarboton (1997). Compared with the D8 algorithm, where the flow is discretized

168   into only one of eight possible directions, separated by 45°, the D∞ algorithm is more

169   reasonable and accurate for delineating the actual river trend.

170   The process of discretizing computational domain based on the D∞ algorithm is

171   shown in Figure 2. First, a raw DEM was prepared, and sink filling was performed on

172   the DEM. Second, the D∞ algorithm was applied to determine the flow direction on

173   grids. Subsequently, the upslope area, defined as the total catchment area that is

174   upstream of a grid center or short length of contour (Moore et al., 1991), was calculated

175   based on the flow direction. Finally, an area threshold was defined to identify the slope

176   lands and derive the river drainage networks from accumulated drainage areas. In a grid

177   cell, if the upslope area was larger than the predefined threshold, it was considered as a

178   river drainage network; otherwise, it was defined as slope lands. The generated slope

179   lands and river network were verified through field surveys or satellite images-based

180   estimates. Generally, the river drainage networks present low slopes and hydraulic

181   conveyance, which is subject to flooding. Therefore, these areas should be discretized

182   using fine grids to represent the flooding process in high resolution. However, in the

183   slope lands, fine grids were not required and coarse grids were used to improve

184   computational efficiency. Because the regions of interest were of high resolution, the

185   reliability of the prediction would not deteriorate, although the number of grid cells was

186   considerably reduced, which can increase model efficiency and capability for flood

187   simulations over large domains. Compared with manual work, the grid generation

188   based on the D∞ algorithm can both reduce workload and time.
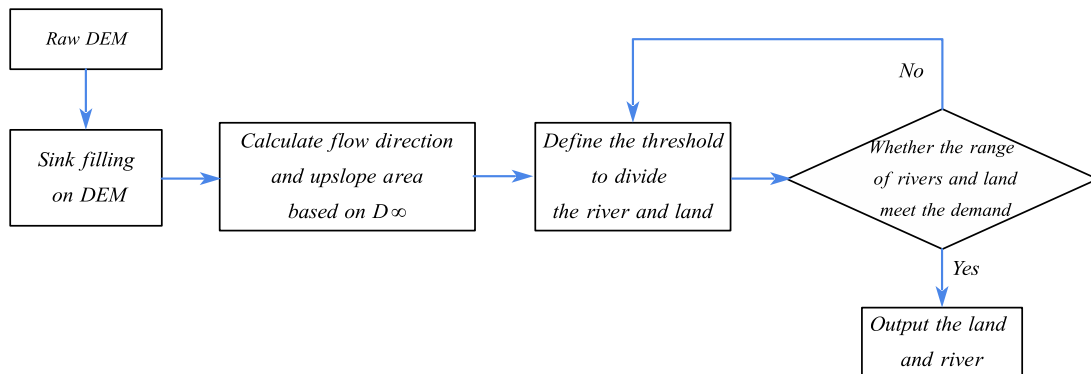
189

190   Figure 2 Grid generation based on the D∞ algorithm

191   A schematic of grid generation is shown in Figure 3. Two types of connecting

192   interfaces are presented, which divide the computing domain into three parts. The first

193   type is the red line (Variable Interpolation Interface, VII) between the coarse and fine

194   grids. The grid cell size changes suddenly on both sides of this line. The second type

195   (Coupling Moving Interface, CMI) is marked in blue on fine grids, which is moving

196   and time-dependent. The first part represents the coarse-grid areas, where the

197   hydrologic model is used to simulate rainfall-runoff. The other two parts are located in

198   the fine-grid areas. The regions between VII and CMI are defined as intermediate

199   transition zones, where the hydrologic model is used to simulate the flooding process.

200   These transition zones facilitate the application of different time steps in different grid

201   cell sizes to improve computational efficiency. The hydrologic and hydrodynamic

202   models are dynamically coupled to represent the flooding process on fine grids, and the

203   CMI is a coupling boundary.
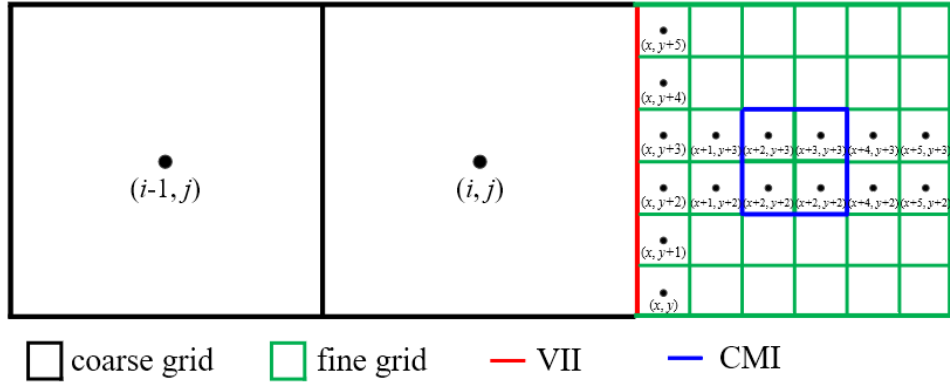
Figure 3. Schematic diagram of grid generation, where i and j are the coordinates of coarse grid; x and y are the coordinates of fine grid; VII is the Variable Interpolation Interface and CMI is the Coupling Moving Interface

2.2 Variable interpolation between coarse and fine grids

During a flow computation, if a cell has a neighbor of different size, interpolation may be required to approximate variables in certain locations so that the governing equation can be solved smoothly. An example is presented in Figure 4(a), where the coarse grid has two eastern neighbors that are half its size. In this case, the variable values of the smaller cells are obtained from those of larger cells. In the traditional method, these variables are directly calculated using certain interpolation methods. There are shared (P_1, P_2) and hanging (Q) nodes at the interface between the coarse and fine grids. In Shen et al. (2021), the variable values on shared nodes can be transmitted directly, while the values on hanging nodes were obtained by linear interpolation of the shared nodes. This method is simple, feasible and easy to use. However, the variable values are stored at the cell center, and there are no values at the interface nodes. Shen et al. (2021) assumed that the values at the interface nodes were equal to that at the cell center. It is inaccurate to make such an assumption, which can bring errors. And the resulting error will increase as the cell size increases.

To overcome these drawbacks, ghost cells and bilinear interpolation method were

10

224   used to interpolate variables between coarse and fine grids. Figure 4(a) shows the

225   variable interpolation between the coarse and fine grids. Two ghost fine cells were

226   created, which were overlaid with partial coarse grids. The variables on the ghost fine

227   cells were interpolated through the coarse and fine grids between the interface, which

228   were then used as the boundary conditions for the calculation of the fine grids at the

229   next time step. The bilinear interpolation method was applied. The variable

230   interpolation may involve variables at locations c_1, c_2, c_3, f_{v1}', f_{v2}', f_1 and f_2. As the

231   variables are stored at the cell center, the variables at c_1, c_2, c_3, f_1 and f_2 are available

232   directly. The values at f_{v1}' and f_{v2}' are obtained via natural neighbor interpolation, as

233   follows:

234
$$U_{f_{v1}'} = U_{c_1} + \frac{U_{c_2} - U_{c_1}}{y_{c_2} - y_{c_1}}(y_{f_{v1}'} - y_{c_1}) \tag{1}$$

235
$$U_{f_{v2}'} = U_{c_3} + \frac{U_{c_1} - U_{c_3}}{y_{c_1} - y_{c3}}(y_{f_{v2}'} - y_{c_3}) \tag{2}$$

236   where $U_{f_{v1}'}, U_{f_{v2}'}, U_{c_1}, U_{c_2}, U_{c_3}$ are the variables at locations $f_{v1}', f_{v2}', c_1, c_2, c_3$ respectively;

237    $y_{f_{v1}'}, y_{f_{v2}'}, y_{c_1}, y_{c_2}, y_{c_3}$ are the coordinates in y directions at $f_{v1}', f_{v2}', c_1, c_2, c_3$ respectively.

238   And then, the variables of ghost fine cells at f_{v1} and f_{v2} can be calculated based

239   on that at f_{v1}' and f_{v2}', as follows:

240
$$U_{f_{v1}} = U_{f_{v1}'} + \frac{U_{f_1} - U_{f_{v1}'}}{x_{f_1} - x_{f_{v1}'}}(x_{f_{v1}} - x_{f_{v1}'}) \tag{3}$$

241
$$U_{f_{v2}} = U_{f_{v2}'} + \frac{U_{f_2} - U_{f_{v2}'}}{x_{f_2} - x_{f_{v2}'}}(x_{f_{v2}} - x_{f_{v2}'}) \tag{4}$$

242   where $U_{f_{v1}}, U_{f_{v2}}$ are the variables of ghost fine cells; U_{f1}, U_{f_2} are the variables at f_1, f_2,

243   respectively, which were calculated in the last time step; $x_{f_1}, x_{f_2}, x_{f_{v1}}, x_{f_{v2}}, x_{f_{v1}'}$ and $x_{f_{v2}'}$

11

244 are the coordinates in x directions at f_1, f_2, f_{v1}, f_{v2}, f_{v1}', f_{v2}' respectively.

245 The values at f_{v1}, f_{v2} were used as the boundary conditions for the calculation of

246 fine grids.

247 The variable interpolation from fine to coarse grids is presented in Figure 4(b),

248 where one ghost coarse cell was established. The variables of ghost coarse cells were

249 determined according to the fine and coarse grids between the interface. The variable

250 interpolation may involve variables at locations c_v', c_1, f_1, f_2. As the variables are stored

251 at the cell center, the variables at c_1, f_1, f_2 are available directly. The values at c_v' are

252 obtained via natural neighbor interpolation, as follows:

$$U_{c_v'} = U_{f_2} + \frac{U_{f_1} - U_{f_2}}{y_{f_1} - y_{f_2}} (y_{c_v'} - y_{f_2}) \tag{5}$$

253

254 where $U_{c_v'}$, U_{f_1}, U_{f_2} are the variables at c_v', f_1, f_2 respectively; $y_{c_v'}$, y_{f_1}, y_{f_2} are the

255 coordinates in y direction at c_v', f_1, f_2 respectively.

256 And then, the variables of ghost coarse cells at c_v can be calculated based on that

257 at c_v', c_1, as follows:

$$U_{c_v} = U_{c_v'} + \frac{U_{c_1} - U_{c_v'}}{x_{c_1} - x_{c_v'}} (x_{c_v} - x_{c_v'}) \tag{6}$$

258

259 where U_{c_v} are the variables of ghost fine cells; U_{c_1} are the variables at c_1, which were

260 calculated in the last time step; x_{c_1}, $x_{c_v'}$, x_{c_v} are the coordinates in x direction at c_1, c_v', c_v

261 respectively.

262 The values at c_v were used as boundary conditions for the calculation of coarse

263 grids at the next time step.
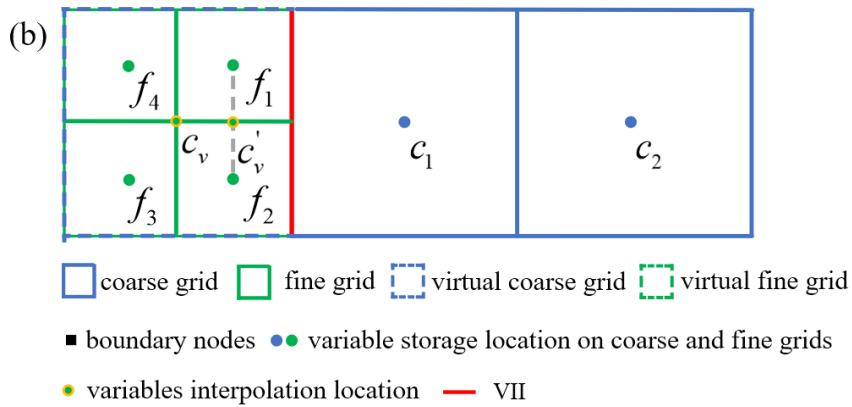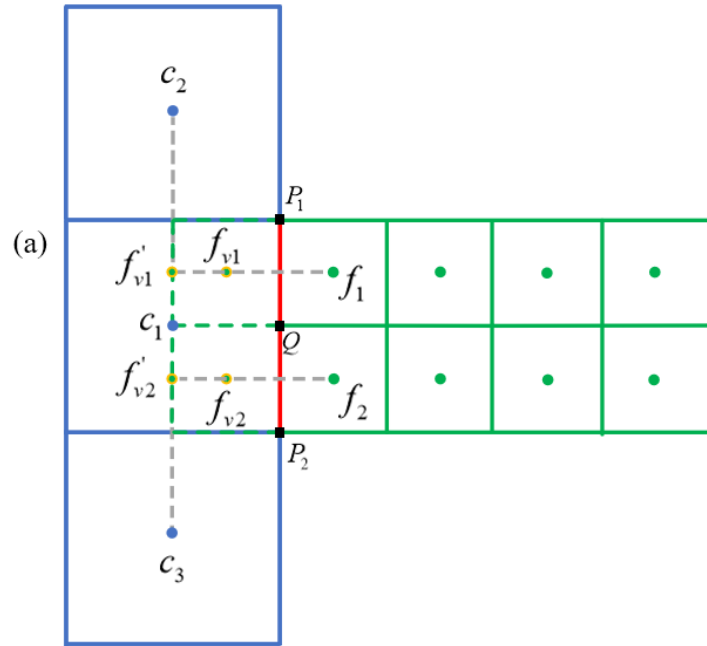
Figure 4. Variables interpolation between coarse and fine grids: (a) from coarse to

fine grids and (b) from fine to coarse grids

On both sides of the interface between coarse and fine grids, the hydrologic model

was used to simulate the flood process. In the hydrologic model applied to the IM-

DBCM, the Manning equation is employed to simulate surface runoff processes. As a

linear partial differential equation, the Manning equation lacks a nonlinear convection

term. Consequently, the flow state undergoes relatively smooth changes without

exhibiting discontinuous solutions. Linear interpolation is applied to interpolate

variables between coarse and fine grids, with the interpolated values falling within the

range defined by the maximum and minimum values of the interval. This interpolation

13

276 ensures that the result lies between these bounds, precluding the occurrence of increased

277 flow at the interface of coarse and fine grid transitions.

278 **2.3 Numerical models**

279 **2.3.1 Hydrologic model**

280 In this study, referring to the runoff calculation in the Storm Water Management

281 Model (SWMM), a 2D NLR model, including water balance and Manning equations,

282 was used to simulate rainfall-runoff. In SWMM, the watershed is divided into many

283 water tanks or reservoirs, where 1D NLR model including water balance and 1D

284 Manning equations is used to simulate the runoff (Rossman, 2015). It is a simple and

285 efficient method to calculate the runoff routing. In reality, however, the runoff routing

286 is a 2D way, so it is not accurate to calculate the 2D runoff routing using 1D NLR model.

287 Also, it is difficult to directly couple the 1D NLR model with 2D hydrodynamic model.

288 Therefore, the 2D NLR model was used to simulate the 2D surface runoff routing in

289 this study, as shown in Eqs. (7-11). The effects of subsurface runoff are assumed to be

290 negligible, which is reasonable for the intense rainfall-induced flood events considered

291 in this study (Hou et al., 2018; Li et al. 2021).

292
$$\frac{V_i^{n+1} - V_i^n}{\Delta t} = \left(Q_x\right)_{in\ i} - \left(Q_x\right)_{out\ i} + \left(Q_y\right)_{in\ i} - \left(Q_y\right)_{out\ i} + A_i q_{r\ i}^n \qquad (7)$$

293
$$\left(Q_x\right)_{in\ i} - \left(Q_x\right)_{out\ i} = -\sum_{l=1}^{L}\left(q_{x\ \Gamma}^n \cdot n_x\right)_l \Delta L_l \qquad (8)$$

294
$$\left(Q_y\right)_{in\ i} - \left(Q_y\right)_{out\ i} = -\sum_{l=1}^{L}\left(q_{y\ \Gamma}^n \cdot n_y\right)_l \Delta L_l \qquad (9)$$

295
$$q_x = \frac{h^{5/3} S_x^{1/2}}{n_r} \qquad (10)$$

296
$$q_y = \frac{h^{5/3} S_y^{1/2}}{n_r} \qquad (11)$$

297 where the superscript n and $n+1$ is the time step; V is the water volume of grid (m^3);

298 $\left(Q_x\right)_{in\ i}, \left(Q_x\right)_{out\ i}$ is the inflow and outflow of grid i in x direction (m^3/s);

299 $\left(Q_y\right)_{in\ i}, \left(Q_y\right)_{out\ i}$ is the inflow and outflow of grid i in y direction (m^3/s); $q_{r\ i}$ indicates

300 runoff rate of grid i (mm/h), which is rainfall intensity minus infiltration rate; A_i is the

301 area of grid i (m^2); q_x, q_y are the unit discharge stored at cell-center along x and y

302 direction (m^2/s), with h, u and v being water depth (m), flow velocity (m/s) in x and y

303 directions, respectively; $q_{x\ \Gamma}, q_{y\ \Gamma}$ are the unit discharge at grid boundary in x and y

304 direction, respectively (m^2/s), which are calculated based on q_x, q_y; ΔL_l is the side

305 length of grid (m); $l = 1, 2, 3, \ldots, L$ is the number of edges of cell; n_r is the Manning

306 roughness coefficient; S_x and S_y are water level gradients along x and y direction,

307 respectively; $S_x = -\partial\left(z_b + h\right)/\partial x$, $S_y = -\partial\left(z_b + h\right)/\partial y$,where z_b is the surface

308 elevation.

309 **2.3.2 Hydrodynamic model**

310 The 2D SWEs, consisting of mass and momentum conservation equations (Toro

311 2001), were used to represent the hydrodynamic model.

312 $$\frac{\partial U}{\partial t} + \frac{\partial F}{\partial x} + \frac{\partial G}{\partial y} = S \tag{12}$$

313 $$U = \begin{pmatrix} h \\ hu \\ hv \end{pmatrix},\ F = \begin{pmatrix} hu \\ huu + gh^2/2 \\ huv \end{pmatrix}, G = \begin{pmatrix} hv \\ huv \\ hvv + gh^2/2 \end{pmatrix}, S = \begin{pmatrix} q_r \\ -gh\dfrac{\partial z}{\partial x} - \dfrac{g}{C^2}u\sqrt{u^2+v^2} \\ -gh\dfrac{\partial z}{\partial y} - \dfrac{g}{C^2}v\sqrt{u^2+v^2} \end{pmatrix}$$

314 where U is the conserved variables; F, G are the convection term in the x and y

315 directions; S is the source term; C is Chezy's coefficient, $C = \dfrac{1}{n_r}R^{1/6}$,where n_r is the

316 Manning roughness coefficient and R is the hydraulic radius.

317　　The Finite Volume Method for Conservative Scheme was used to solve the SWEs,

318 which can ensure local mass and momentum conservation in each control volume cell.

319 The Eq. (12) can be discretized based on structured grids, as follows:

$$320 \qquad U_{i,j}^{n+1} = U_{i,j}^{n} - \frac{\Delta t}{A_{i,j}} \sum_{l=1}^{L} \left[F^{l}\left(U_{i,j}^{n}\right)dy - G^{l}(U_{i,j}^{n})dx \right] + \frac{\Delta t}{A_{i,j}} S\left(U_{i,j}^{n}\right) \qquad (13)$$

321 where the superscript n and $n+1$ is the time step; the subscript i, j refers to the grid i, j;

322 dx and dy are the grid edge length. The meaning of other symbols is the same as before.

323　　The Harten-Lax-van Leer contact (HLLC) approximate Riemann solver was used

324 to solve the convection term. The second-order accuracy in temporal and spatial

325 discretization was obtained based on the Runge-Kutta method and Monotone

326 Upstream-centered Schemes for Conservation Laws (MUSCL) (Van Leer, 1979). The

327 solution of SWEs was detailed in many references (Toro 2001).

328 **2.4 Dynamic bidirectional coupling of hydrologic and hydrodynamic models**

329　　The hydrologic and hydrodynamic models were coupled dynamically and bi-

330 directionally. A water depth threshold was defined in advance and used to determine

331 the state of the cell. In a grid cell, if the water depth was lower than the predefined

332 threshold, it was defined as a non-inundation region where the hydrologic model was

333 applied. Conversely, if the water depth was higher than the threshold, it was considered

334 an inundation region where the 2D hydrodynamic model was applied. When the rainfall

335 intensity increased, the water depth increased because of the gradual accumulation of

336 surface water volume. Once the water depth exceeds the predefined threshold, the non-

337 inundation regions defined last time step may change to the inundation regions. The

338 inflow discharge positions, flow path, and discharge values subsequently changed.

339 Therefore, a CMI was formed between the inundation and non-inundation regions and

340   the hydrologic and 2D hydrodynamic models were coupled bi-directionally through this

341   CMI.

342   The hydrologic model is rational for the continuous non-inundation regions, and

343   the hydrodynamic model is rational for the continuous inundation regions. However,

344   since discontinuity existed at the CMI, the single hydrologic or hydrodynamic models

345   were not acceptable, which was a challenge for the model calculation, as shown in

346   Figure 5. The key issue with the coupled model was to establish a reasonable approach

347   for determining the fluxes passing through the coupling interface, which should

348   integrate the effect of the current flow state obtained from these two models on both

349   sides of the coupling interface.

Non-inundation regions   **CMI**   Inundation regions
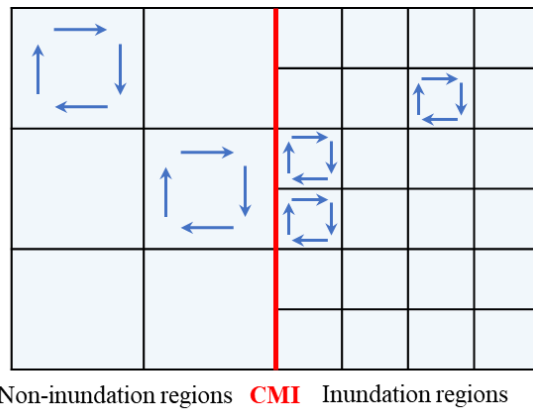
350

351   Figure 5 Model calculation at inundation regions, non-inundation regions and CMI

352   A pair of characteristic waves was used to determine the fluxes calculation

353   methods through the CMI. The characteristic waves were calculated as follows:

$$S_L = u_{i,j} - \sqrt{gh_{i,j}} \tag{1}$$

$$S_R = u_{i+1,j} - \sqrt{gh_{i+1,j}} \tag{2}$$

356   where S_L and S_R are the characteristic waves; u is the flow velocity (m/s); h is the

357   water depth (m); subscript (i, j) and $(i+1, j)$ refer to the cells in non-inundation and

358   inundation regions, respectively.

359   If $S_R > 0$ and $S_L > 0$, the fluxes through the CMI were calculated by the

360   hydrologic model, and the CMI may move toward the non-inundation regions.

361   Therefore, the non-inundation regions shrunk, whereas the inundation regions

362   expanded. Only mass conservation through the CMI can be considered in this situation.

363   If $S_L < 0 < S_R$, the fluxes were calculated by both hydrologic and hydrodynamic

364   models, and the CMI remained unchanged.

365   If $S_L < 0$ and $S_R < 0$, the fluxes are calculated by the hydrodynamic model, and

366   the CMI may move toward inundation regions. Therefore, the inundation regions

367   shrunk, whereas the non-inundation regions expanded. Both the mass and momentum

368   conservation through the coupling boundary were obtained in the latter two situations.

369   The couplings were detailed in Jiang et al. (2021) and Shen et al. (2021).

370   **2.5 Time step**

371   An explicit scheme was used to solve the hydrologic and hydrodynamic models

372   over time. The time step was constrained by the Courant-Friedrichs-Lewy condition

373   (Delis and Nikolos, 2013), where the time step was a dynamic adjustment based on the

374   velocity and water depth in the computational domain. Different time steps were

375   adopted for the coarse and fine grids, and the time step of the fine grids was determined

376   as follows:

377
$$\Delta t_f = C \cdot min\left(\frac{min\left(\Delta x_f\right)}{max\left(\left|u_f\right| + \sqrt{gh_f}\right)}, \frac{min\left(\Delta y_f\right)}{max\left(\left|v_f\right| + \sqrt{gh_f}\right)} \right) \tag{14}$$

378   where Δt_f is the time step of fine grids; C is a constant used to maintain format stability;

379   Δx_f and Δy_f are the side lengths of fine grid in x and y directions; u_f and v_f are the

380   flow velocities on fine grids along x and y directions, respectively; h_f is the water depth

381   on fine grids.

382   The time step of the coarse grids (Δt_c) was determined based on that of the fine

383   grids. If the size of the coarse grid was k times that of the fine grid, the time step of the

384   coarse grid was determined to be $\Delta t_c = k\Delta t_f$.

385   3 Results

386   The performance of the IM-DBCM was analyzed by applying it to two 2D rainfall-

387   runoff experiments and one real-world flooding process. And the OM-DBCM

388   developed by Shen et al. (2021) was applied to the same cases for comparison with the

389   IM-DBCM.

390   3.1 Rainfall over a plane with varying slope and roughness

391   In this case, a sloping plan measuring $500m \times 400m$ was designed, with slopes

392    $S_{ox} = 0.02 + 0.0000149x$ and $S_{oy} = 0.05 + 0.0000116y$ along the x and y directions,

393   respectively (Jaber and Mohtar, 2003). The Manning coefficient is equal to

394    $n = \sqrt{n_x^2 + n_y^2}$, where $n_x = 0.1 - 0.0000168x$ and $n_y = 0.1 - 0.0000168y$. The rainfall

395   intensity is given by a symmetric triangular hyetograph $r = r(t)$,with

396    $r(0) = r(200\,\text{min}) = 0$ and $r(100\,\text{min}) = 0.8 \times 10^{-5}\,m/s$. The total simulation time was

397   14,400 s.

398   Different cases with various grid resolutions were developed to divide the

399   computational domain based on the D∞ algorithm, as listed in Table 1. In these cases,

400   the size of all the fine grids was $1m \times 1m$. The grid discretization of different cases is

401   shown in Figure S1 in Supplement.

402   Table 1 Different cases designed to simulate

Cases	The ratio of coarse to fine grids	Number of grids
case12	1:2	112,100
case15	1:5	86,840
case10	1:10	83,220

403   The hydrographs at the outlet node of coordinates of (500m, 400m) obtained from

404   different models are shown in Figure 6. A model proposed by Jaber and Mohtar (2003)

405   was also used to simulate the overland runoff. Because finer grids and small time step

406   were used to divide the computational domain to obtain more accurate results in the

407   model developed by Jaber and Mohtar (2003), the results calculated by Jaber and

408   Mohtar (2003) can be used as a reference solution.

409   From Figure 6, the IM-DBCM held a shape close to the results simulated by Jaber

410   and Mohtar (2003) in all cases, as well as the peak discharge. But the peak discharge

411   of the hydrograph is slightly overestimated by the OM-DBCM, which may be attributed

412   to the difference in the variable interpolation between the coarse and fine grids. In the

413   OM-DBCM, variables at the interpolation interface were equal to that at the cell center,

414   which was then used to interpolate variables between the coarse and fine grids through

415   shared and hanging nodes. This interpolation method had two drawbacks. Firstly, it is

416   not reasonable to assume the variables at the interpolation interface are equal to that at

417   the cell center, and the resulting error could increase as the grid size increases. Besides,

418   compared with bilinear interpolation, the values at the hanging nodes are calculated by

419   linear interpolation through shared nodes, which may result in relatively large errors.

420   The results show that the methods to interpolate variable between the coarse and fine

421   grids by developing ghost cells proposed in this study has acceptable accuracy.

422   To quantitatively assess the performance of IM-DBCM, the Root Mean Square

423   Error (RMSE) of different cases was computed. The RMSEs of case12, case15 and

424   case10 were 4.01E-04, 7.85E-03 and 3.25E-02, respectively. It is showed that the error

425   gradually increased with the increasing of the ratio of coarse to fine grids. The IM-

426   DBCM may capture the shape of the hydrograph in case12 and case15, both in limbs

427   and peak discharge, but the peak discharge is slightly underestimated in case10. A

428 possible explanation is that, compared to the coarse grids, the fine grids could better

429 capture the geometry of the channel cross-sections. High-resolution grids can better

430 represent small-scale topographic features and flow passages (Hou et al., 2018);

431 consequently, the simulation results on case12 and case15 are more satisfactory than

432 those on case10. Similarly, the simulation accuracy of the OM-DBCM also gradually

433 decreased with the increasing of the ratio of coarse to fine grids. Overall, the benefit of

434 using the IM-DBCM for the flood simulations is evident.

435

436
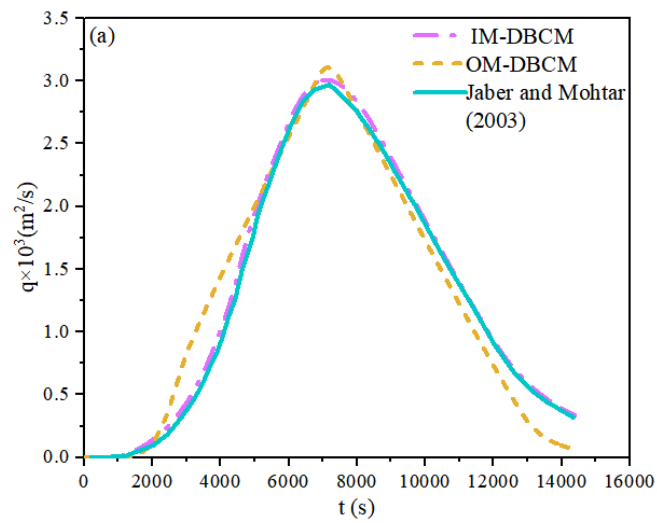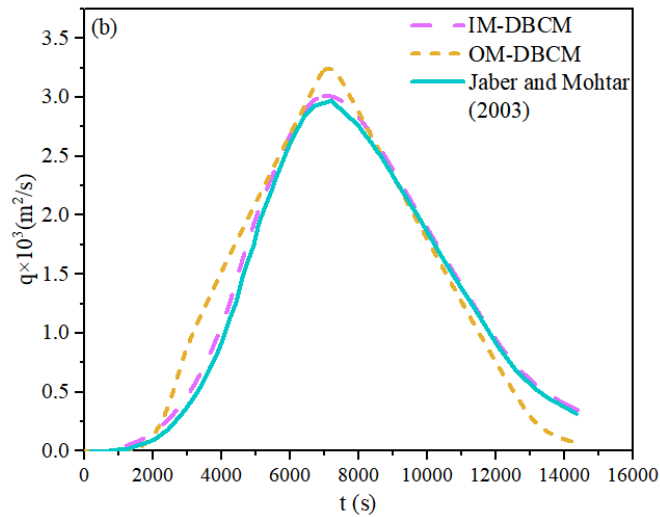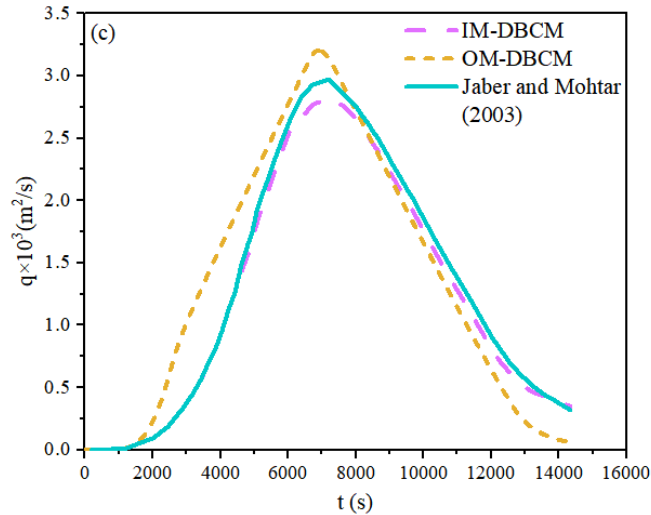
Figure 6 Hydrographs obtained from different models: (a) case12, (b) case15 and (c) case10

3.2 V-shaped catchment

A 2D surface flow simulation was conducted over a V-shaped catchment to evaluate the performance of the IM-DBCM. The computational domain is symmetrically V-shaped, with two symmetrical hillslopes converging to form a channel in the central region. The river bed slopes -0.05 on the left side and 0.05 on the right side. The channel bed has zero slope in the x direction and a slope of 0.02 in the y direction. The Manning coefficient is 0.015 on the hillslope and 0.15 on the main channel. The detailed dimensions and associated information pertaining to the V-shaped catchment are presented in Figure 7. The total simulation time was 10,800 s, with a constant rainfall intensity of 10.8 mm/h applied for 5,400 s.
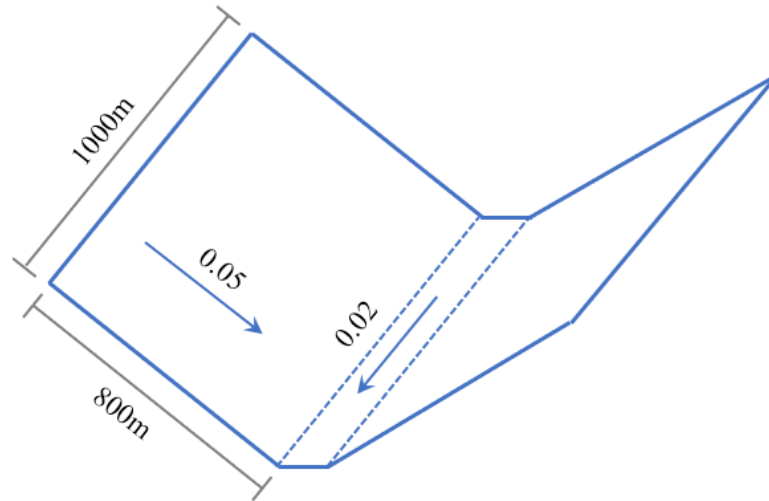
Figure 7. Geometry and size of the V-shaped catchment

The IM-DBCM was used to simulate the 2D surface flow over the V-shaped domain. The computational basin was divided into coarse and fine grids based on the D∞ algorithm. The size of the fine grids was 10m × 10m, whereas that of the coarse grids was 20m × 20m. The grid partition is presented in Figure S2 in Supplement, where a V-shaped zones near the watershed outlet was discretized using fine grids, while the remaining areas were discretized using coarse grids.

Besides, the HM2D and the coupled Mike SHE and Mike 11 was also developed to simulate the surface flow under the same conditions. In the HM2D, the grid size was set as 10m × 10m. In the coupled Mike SHE and Mike 11, the Mike SHE was used to simulate the rainfall-runoff on the hillslopes and the grid sizes was also 10m × 10m, while the Mike 11 was used to simulate the runoff in the channel. Results were all compared with measured data.

The discharge hydrographs obtained from different models are shown in Figure 8. This figure showed a close match between the measured data and the computed results obtained using the IM-DBCM. This indicated that the results were encouraging and the overall trend was well captured. The hydrographs obtained from the IM-DBCM was closer to the analytical solution compared with the coupled Mike SHE and Mike 11.

469   The weir flow equation was utilized to couple the Mike SHE and Mike 11. Notably,

470   only mass was transferred between the models, excluding momentum. However, mass

471   and momentum were exchanged between the hillslopes and river channels. The IM-

472   DBCM model ensured the conservation of both mass and momentum, resulting in

473   simulated hydrographs that closely match analytical solutions.

474   Comparing the hydrographs generated by the 2D hydrodynamic model and IM-

475   DBCM, the discharge hydrographs exhibited congruence for the discharge receding

476   limb and peak discharge. However, the consistency of the hydrographs simulated by

477   these two models was less pronounced for the rising limb. In the rising limb, the flow

478   calculated using IM-DBCM was lower than that simulated using HM2D. The disparity

479   in hydraulic behavior between the hydrodynamic and hydrologic models explains the

480   observed phenomenon. The HM2D consistently simulate the surface flow using the 2D

481   hydrodynamic model; conversely, the hydrologic model was employed solely to

482   simulate the flood processes when the upstream water level recedes below the threshold

483   established in IM-DBCM. In the hydrologic models that lack time-partial derivative

484   terms, the current velocity was solely determined by the instantaneous water level

485   gradient. This differs from the previous calculation method, which added the flux term

486   to the velocity at the previous time step. Consequently, the velocity calculation in 2D

487   hydrodynamic models deviated from the IM-DBCM.
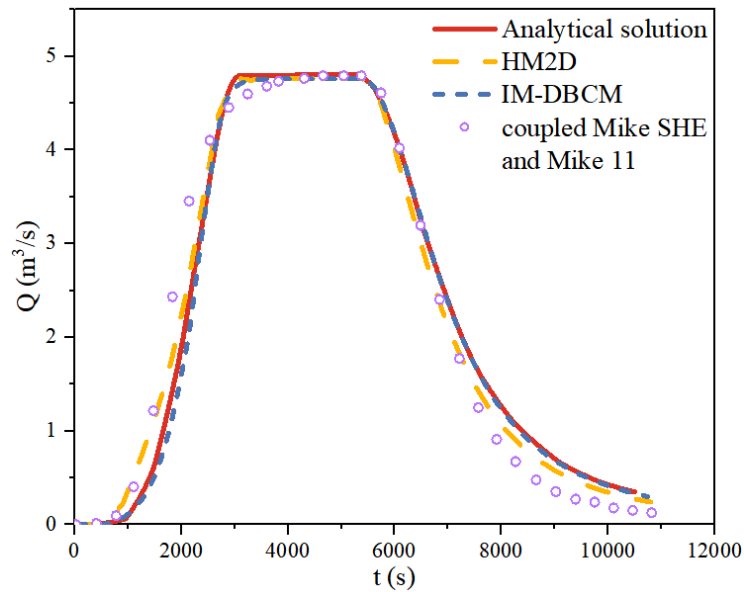
Figure 8. Measured and simulated results obtained from different models

3.3 Flood simulation in a natural watershed

The Goodwin Creek watershed, located in Panola County, Mississippi, USA, is often selected as a benchmark to assess the capability of flood models because of sufficient available observed data. Drainage is westerly to Long Creek which flows into the Yocona River, one of the main rivers of the Yazoo River, a tributary of the Mississippi River. The Goodwin Creek watershed covers an area of 21.3 km^2. The overall terrain gradually decreased from northeast to southwest, which is consistent with the trend of the main channel, and the elevation ranged from 71 to 128 m. The computational basin and bed elevations are shown in Figure9.

Land use in this watershed was divided into four classes including forest, water, cultivated, and pasture, and their Manning coefficients were 0.05, 0.01, 0.03, and 0.04, respectively (Sánchez, 2002). The infiltration coefficients of different soil types were determined according to Blackmarr (1995). The rainfall event in sixteen rain gages (see Figure 9) of October 17, 1981 was chosen for simulation (Sánchez, 2002), and the inverse distance interpolation method (Barbulescu, 2016) was used to calculate the precipitation over the entire watershed. The rainfall duration was 4.8 h. Rainfall was

25

spatially distributed at different times, as shown in Figure S3 in Supplement. There were measured data in six observation stations (i.e., 1, 4, 6, 7, 8 and 14) (Blackmarr, 1995), whose locations were shown in Table S1 in Supplement, and the simulated results were compared with the measured data in these stations.
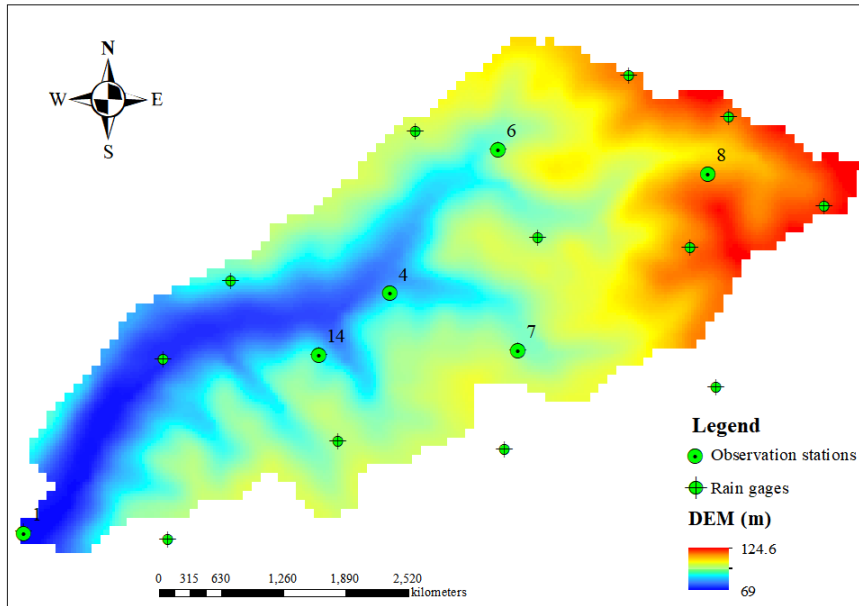
Figure 9. Overview of the Goodwin Creek watershed

The simulations were performed for 12 h. Different cases with various grid resolutions were developed to verify the computational efficiency and numerical accuracy of IM-DBCM, as listed in Table 2. In M-DBCM, the rivers were covered by fine-grid cells with dimensions of 10 m $\times$ 10 m, whereas the coarseness in the rest of the domain was increased to higher levels, as presented in Figure S4 in Supplement.

Table 2. Different cases designed to simulate the Goodwin Creek watershed

Cases	The ratio of coarse to fine grids	Number of grids
case12	1:2	104,555
case15	1:5	65,240
case10	1:10	59,431

The OM-DBCM was also used to simulate the rainfall runoff with the same resolutions. The Nash-Sutcliffe efficiency (NSE) was used to quantify errors in each

26

520   model. The NSEs of IM-DBCM and OM-DBCM are shown in Table 3. From this table,

521   the NSEs of IM-DBCM were higher than that of OM-DBCM at most stations, which

522   was probably caused by the different interpolation method at the interface between

523   coarse and fine grids. It is verified that the IM-DBCM has relatively high accuracy in

524   simulating rainfall-runoff. In OM-DBCM, it is unreasonable to make the variables at

525   the interface between coarse and fine grids equal to that at the cell center, which can

526   bring errors. The induced error will increase as the ratio of coarse and fine grids increase.

527   Therefore, it is also observed that the NSEs of OM-DBCM decreased with the increased

528   ratio of coarse and fine grids. It is indicated that the ghost cells and bilinear interpolation

529   used in the IM-DBCM to interpolate variables between coarse and fine grids can make

530   the simulation more reasonable.

531   Table 3 NSEs of different models ("IM" and "OM" refer to IM-DBCM and OM-

532   DBCM, respectively)

| Station	G1		G4		G6		G7		G8		G14	
Model	IM	OM	IM	OM	IM	OM	IM	OM	IM	OM	IM	OM
case12	0.9496	0.9108	0.9611	0.9011	0.9904	0.8982	0.9658	0.9004	0.9435	0.9104	0.9311	0.8804
case15	0.9399	0.8766	0.9404	0.8800	0.9426	0.8819	0.9258	0.8931	0.9341	0.8942	0.9001	0.7942
case10	0.9207	0.8261	0.8907	0.8435	0.9513	0.7977	0.9358	0.8525	0.9358	0.8678	0.9135	0.8078

533   Figure 10 shows a comparison of the measured and simulated hydrographs by IM-

534   DBCM at the monitoring gauges, whose locations are presented in Figure 10. At all

535   gauges, the hydrographs obtained from different cases were well aligned with the

536   measured data, which indicates that the IM-DBCM could reliably reproduce the flood

537   wave propagation in the complex topography. The results of case12, in general, were

538 better than those of case15 and case10, especially at station G1. A possible explanation

539 is that a finer grid is needed to better capture the watershed geometry and obtain more

540 satisfactory simulation accuracy. The cell size of case15 and case10 is larger than that

541 of case12.

542   Compared with other stations, at station G1, the simulation results obtained from

543 case15 and case10 deviated substantially from the measured data, especially at receding

544 limb of the hydrographs. We deduced that the reason for this discrepancy is not the

545 mesh partitioning, but the location of the G1. G1 is located at the watershed outlet,

546 where water flows out of the watershed from here. The errors generated upstream may

547 be accumulated at this station. Despite the deviation, the overall trend of the

548 hydrographs indicated that the IM-DBCM is satisfactory and can reliably reproduce

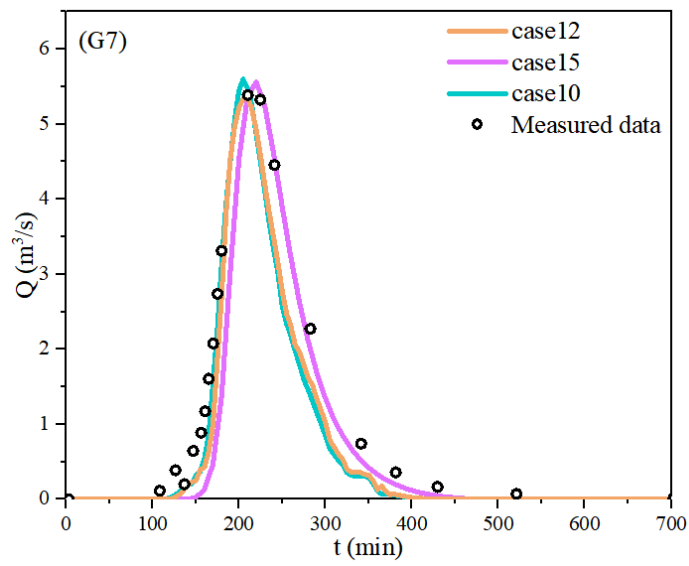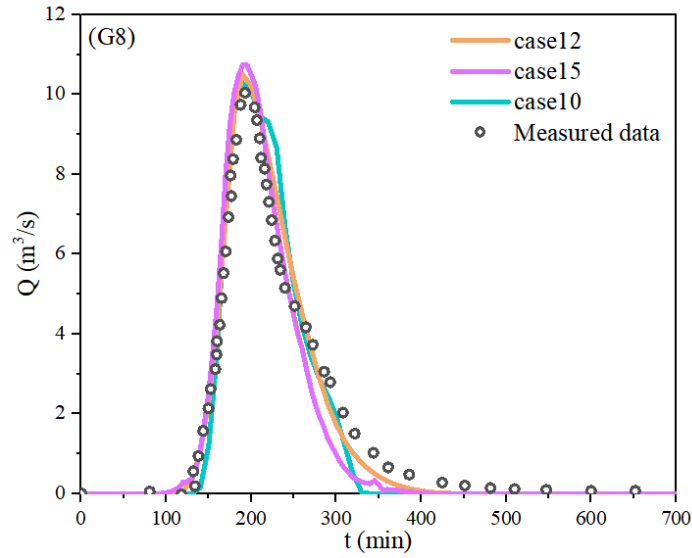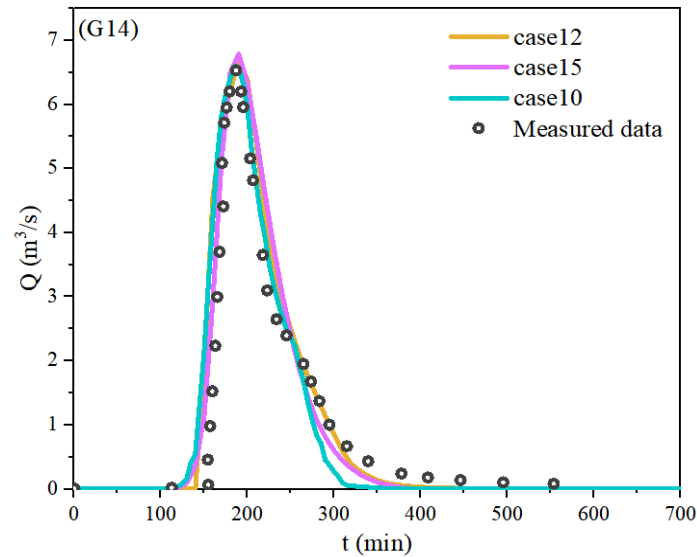549 flood wave propagation in complex topography.
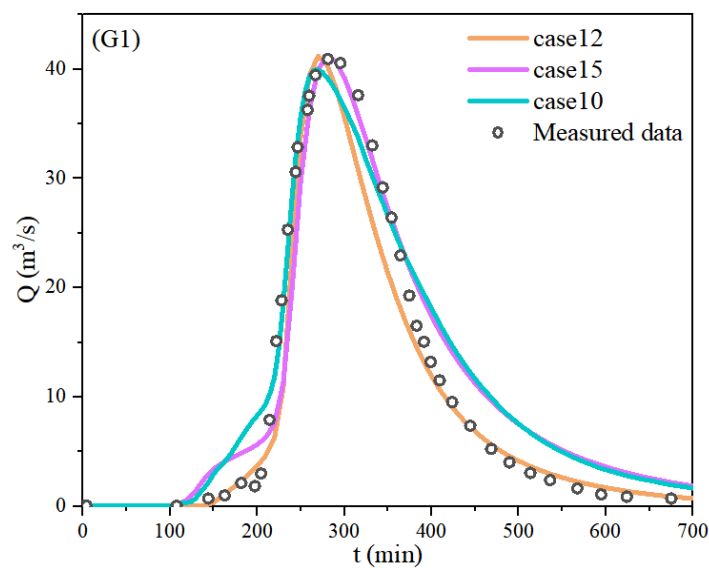
550

551

552

553

554

555
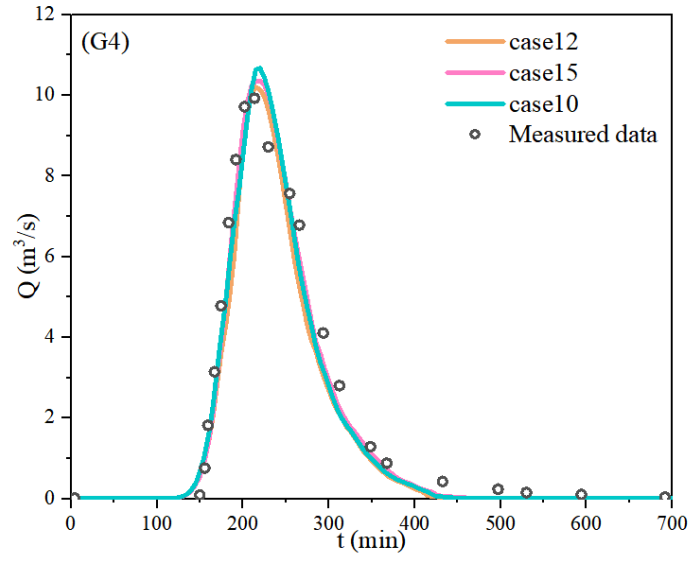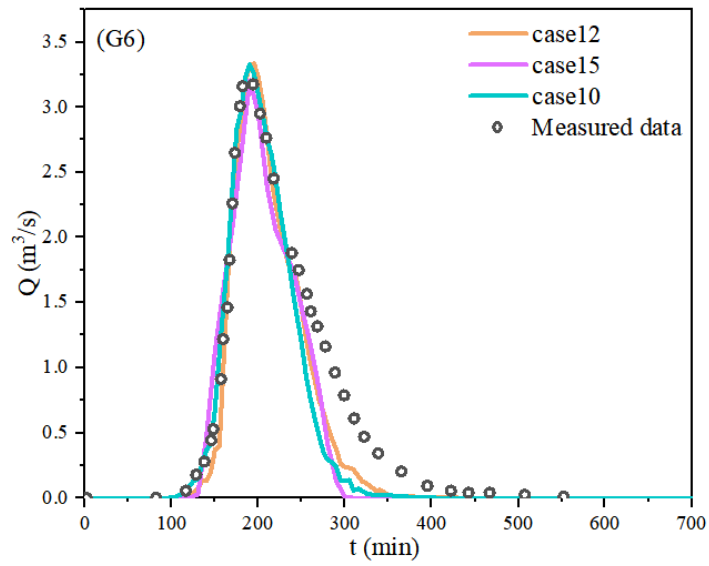
Figure 10. Hydrographs obtained from different cases

In terms of efficiency, the total execution time of IM-DBCM was compared with the uniform grid-based model (HM2D), as shown in Figure 11. The total execution time of the different cases ranked from highest to lowest is as follows: HM2D> case12> case15> case10. Compared to HM2D, the multi-grid discrete computing domain improves computational efficiency by 60%. Uniform fine grids were used to divide the computing zones in HM2D, and 207,198 computational grids were generated. Compared with HM2D, most of the areas were discretized with coarse grids, and only a small part of the regions was calculated based on fine grids in IM-DBCM; the

computational grids of the multi-grid-based model (Table 2) were considerably lower than that of HM2D. Furthermore, case12 required more computational time than case15 and case10. Fewer computational grid nodes were presented in case15 and case10, which required less time for calculation, and the computational efficiency could be further improved. The advantages of using IM-DBCM based on multi-grids for flood simulations are evident. The difference in total runtime between the IM-DBCM and OM-DBCM is the time spent on mesh generation. In the OM-DBCM, the computational domain is divided manually, which is highly subjective, and the computational time varied from person to person.

However, there was not a significant difference in the computation time among case12, 15 and 10. The calculation time for coarse grids is shown in Figure 11(b). It is observed that the runtime for coarse grids decreases rapidly in different cases. In case12, case15 and case10, the number of coarse grids is 42517, 7425, and 2153, respectively. As the number of coarse grids decreased significantly, the runtime for these grids also decreased rapidly. The number of fine grids is consistent in case12, case15, and case10, with a calculation time of 4800s. The fine grids number is much greater than that of the coarse grids, especially in case15 and case10. The 2D hydrodynamic model was solved in the fine-grid regions, which cost more computation time compared with the coarse grids where the hydrologic model was applied. The calculation time for fine grids is significantly longer than that for coarse grids, comprising a substantial portion of the overall execution time.

In many watersheds, the 2D inundation regions account for a minor proportion of the total watershed area. The fine grids were employed to partition the small inundation regions, while the coarse grids were utilized to discretize the majority of the non-inundation regions. The computational efficiency can be significantly enhanced due to

590   the smaller proportion of fine grids and larger proportion of coarse grids. In the IM-

591   DBCM, the 1D rivers and 2D inundation regions were not distinguished, resulting in

592   their division using fine grids. Consequently, the 2D hydrodynamic model was applied

593   to both regions, leading to an increased computational time. In future studies, the 1D

594   hydrodynamic model will be used to compute the flood evolution specifically in the 1D

595   rivers, leading to a reduction in computational time. Hence, the computational

596   efficiency advantages of the proposed IM-DBCM are more pronounced.
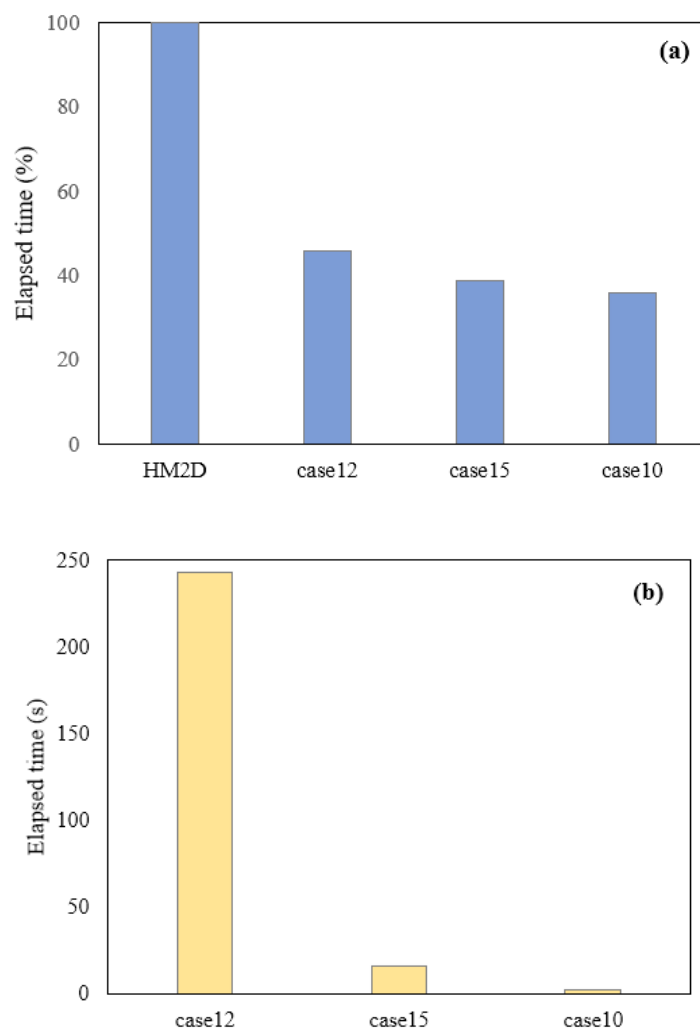
597

598

599   Figure 11. Computation time of different cases: (a) the relative difference of HM2D

600   and IM-DBCM; (b) the runtime for coarse grids

601   **4 Conclusions**

602   An improved dynamic bidirectional coupled hydrologic-hydrodynamic model

603   based on multi-grid (IM-DBCM) was presented in this study. A multi-grid system was

604   generated based on the D∞ algorithm, dividing regions that required high-resolution

605   representation using fine grids and the rest using coarse grids to reduce computational

606   load. A two-dimensional non-linear reservoir was adopted in the hydrologic model,

607   while two-dimensional shallow water equations were applied in the hydrodynamic

608   model. The hydrologic model was applied to the coarse-grid regions, whereas the

609   hydrologic and hydrodynamic models were coupled in a bidirectional manner for the

610   fine-grid areas. Different time steps were adopted in coarse and fine grids. Ghost cells

611   and bilinear interpolation were used to interpolate variables between coarse and fine

612   grids. The hydrologic and hydrodynamic models were dynamically and bidirectionally

613   coupled with a time-dependent and moving coupling interface.

614   The performance of IM-DBCM was verified using three cases. The IM-DBCM

615   was demonstrated to effectively simulate flow processes and ensure reliable simulation.

616   Compared with the OM-DBCM, the results obtained from the IM-DBCM were well

617   aligned with the measured data, and it could reliably reproduce the flood wave

618   propagation in complex topography. In addition to producing numerical results with

619   similar accuracy, the IM-DBCM saved computational time compared with the model

620   on fine grids. Furthermore, a moving coupling interface between the hydrologic and

621   hydrodynamic models was observed in the IM-DBCM. The IM-DBCM has both high

622   computational efficiency and numerical accuracy, which was adapted adequately to the

623   real-life flooding process and provided practical and reliable solutions for rapid flood

624   prediction and management, especially in large watersheds.

625   The IM-DBCM accurately and efficiently reproduces the flooding process and has

626   the potential for a wide range of practical applications. The hydrologic model considers

627   only surface runoff, which is appropriate for the intense rainfall-induced flood events

628 examined in this study. However, a complete hydrologic model should include surface

629 flow, interflow, and underground runoff. In future works, the interflow and

630 underground runoff could be calculated in the hydrologic model.

631 **Data availability**

632 Model simulation and calibration data are available upon request from the

633 corresponding author. Digital elevation model data are provided by the Geospatial Data

634 Cloud at http://www.gscloud.cn. The data sets of Soil Properties and Land cover are

635 provided by Sánchez (2002) and Blackmarr (1995). The rainfall and measured data

636 were Blackmarr (1995).

637 **Author contributions**

638 Yanxia Shen designed the methodology and carried out the investigation. Qi Zhou

639 provided the original model input data. The study was supervised by Chunbo Jiang.

640 Yanxia Shen prepared the first draft of the manuscript and Zhenduo Zhu revised and

641 improved the original manuscript.

642 **Competing interests**

643 The authors declare that they have no conflict of interest.

644 **Acknowledgements**

649 **References**

650 Barbulescu, A.: A new method for estimation the regional precipitation. Water

651 Resources Management, 30(1), 33-42, 2016. https://doi.org/10.1007/s11269-015-

652 1152-2

653   Bates, P.D.: Flood inundation prediction. Annual Review of Fluid Mechanics, 54:287-

654   315, 2022. https://doi.org/10.1146/annurev-fluid-030121-113138

655   Bhola, P.K., Leandro, J., Disse, M.: Framework for offline flood inundation forecasts

656   for two-dimensional hydrodynamic models. Geosciences (Switzerland), 8(9), 346,

657   2018. https://doi.org/10.3390/geosciences8090346

658   Blackmarr, W.: Documentation of hydrologic, geomorphic, and sediment transport

659   measurements on the Goodwin Creek experimental watershed, northern

660   Mississippi, for the period 1982-1993. Technical Report for United States

661   Department of Agriculture: Oxford, MS, USA, October, 1995.

662   Bomers, A., Schielen, R.M.J., Hulscher, S.J.M.H.: The influence of grid shape and grid

663   size on hydraulic river modelling performance. Environmental Fluid Mechanics.

664   19(5), 1273-1294, 2019. https://doi.org/10.1007/s10652-019-09670-4

665   Cea, L, Puertas, J., Pena, L., Garrido, M.: Hydrologic forecasting of fast flood events

666   in small catchments with a 2D-SWE model, Numerical model and experiment

667   validation. World Water Congress, 1-4, Montpellier, France, 2008.

668   Caviedes-Voullième, D., García-Navarro, P., Murillo, J.: Influence of mesh structure

669   on 2D full shallow water equations and SCS curve number simulation of

670   rainfall/runoff events. Journal of Hydrology, 448-449(2), 39-59, 2012.

671   https://doi.org/10.1016/j.jhydrol.2012.04.006

672   Choi, C.C., Mantilla, R.: Development and Analysis of GIS Tools for the Automatic

673   Implementation of 1D Hydraulic Models Coupled with Distributed Hydrological

674   Models. Journal of Hydrologic Engineering, 20, 06015005, 2015.

675   https://doi.org/10.1061/(ASCE)HE.1943-5584.0001202

676   Costabile, P., Costanzo, C.: A 2D-SWEs framework for efficient catchment-scale

677   simulations: hydrodynamic scaling properties of river networks and implications

678   for non-uniform grids generation. Journal of Hydrology, 599(6402), 126306, 2021.

679   https://doi.org/10.1016/j.jhydrol.2021.126306

680   Chen, W., Huang, G., Han, Z.: Urban stormwater inundation simulation based on

681   SWMM and diffusive overland-flow model. Water Science and Technology

682   76(12):3392-3403, 2017. https://doi.org/10. 2166/wst.2017.504

683   Chen, W., Huang, G., Han, Z., Wang, W.: Urban inundation response to rainstorm

684   patterns with a coupled hydrodynamic model: a case study in Haidian Island,

685   China. Journal of Hydrology 564:1022–1035, 2018.

686   https://doi.org/10.1016/j.jhydrol.2018.07.069

687   Delis, A., Nikolos, I.: A novel multidimensional solution reconstruction and edge-based

688   limiting procedure for unstructured cell-centered finite volumes with application

689   to shallow water dynamics. International Journal for Numerical Methods in Fluids,

690   71: 584-633, 2013. https://doi.org/10.1002/fld.3674

691   Donat, R., Marti M.C., Martinez-Gavara, A., Mulet P.: Well-balanced adaptive mesh

692   refinement for shallow water flows. Journal of Computational Physics, 257:937-

693   53, 2014. https://doi.org/10.1016/j.jcp.2013.09.032

694   Ding, Z.L., Zhu, J.R., Chen, B.R., Bao, D.Y.: A Two-Way Nesting Unstructured

695   Quadrilateral Grid, Finite-Differencing, Estuarine and Coastal Ocean Model with

696   High-Order Interpolation Schemes. Journal of Marine Science and Engineering,

697   9(3), 335, 2021. https://doi.org/10.3390/jmse9030335

698   Feistl, T., Bebi, P., Dreier, L., Hanewinkel, M., Bartelt, P.: A coupling of hydrologic

699   and hydraulic models appropriate for the fast floods of the Gardon river basin

700   (France). Natural Hazards & Earth System Sciences, 14(11), 2899-2920, 2014.

701   https://doi.org/10.5194/nhess-14-2899-2014

702   Garcia-Navarro P., Murillo J., Fernandez-Pato J., Echeverribar I., Morales-Hernandez

M.: The shallow water equations and their application to realistic cases. Environmental fluid mechanics. 19(5): 1235-1252, 2019. https://doi.org/10.1007/s10652-018-09657-7

Ghazizadeh, M.A., Mohammadian, A., Kurganov, A.: An adaptive well-balanced positivity preserving central-upwind scheme on quadtree grids for shallow water equations. Computers & Fluids. 208, 104633, 2020, https://doi.org/10.1016/j.compfluid.2020.104633

Hu, R., Fang, F., Salinas, P., Pain, C.C.: Unstructured mesh adaptivity for urban flooding modelling. Journal of Hydrology 560,354-363, 2018. https://doi.org/10.1016/j.jhydrol.2018.02.078

Hou, J., Wang, R., Liang, Q., Li, Z., Huang, M.S., Hinkelmann, R.: Efficient surface water flow simulation on static cartesian grid with local refinement according to key topographic features. Computers & Fluids, 176, 117-134, 2018. https://doi.org/10.1016/j.compfluid.2018.03.024

Hou J., Liu F., Tong Y., Guo K., Li D.: Numerical simulation for runoff regulation in rain garden using 2D hydrodynamic model. Ecological Engineering, 153(2), 105794, 2020. https://doi.org/10.1016/j.ecoleng.2020.105794

Jaber, F.H., Mohtar, R.H.: Stability and accuracy of two-dimensional kinematic wave overland flow modeling. Advances in Water Resources, 26(11): 1189-1198, 2003. https://doi.org/10.1016/S0309-1708(03)00102-7

Jiang, C., Zhou, Q., Yu, W., Yang, C., Lin, B.: A dynamic bidirectional coupled surface flow model for flood inundation simulation. Natural Hazards and Earth System Sciences, 21(2), 497-515, 2021. https://doi.org/10.5194/nhes-21-497-2021

Kim, J., Warnock, A., Ivanov, V.Y., Katopodes, N.D.: Coupled Modeling of Hydrologic and Hydrodynamic Processes Including Overland and Channel Flow.

728 Advances in Water Resources, 37, 104-126, 2012.

729 https://doi.org/10.1016/j.advwatres.2011.11.009

730 Kesserwani, G., Sharifian, M.K.: (Multi)wavelet-based Godunov-type simulators of

731 flood inundation: Static versus dynamic adaptivity. Advances in water resources,

732 171,104357, 2023. https://doi.org/10.1016/j.advwatres.2022.104357

733 Li, Z., Chen, M.Y., Gao, S., Luo, X.Y., Gourley, J.J., Kirstetter, P., Yang, T.T., Kolar,

734 R., McGovern, A., Wen, Y.X., Rao, B., Yami, T., Hong, Y. (2021). CREST-IMAP

735 v1.0: a fully coupled hydrologic-hydraulic modeling framework dedicated to flood

736 inundation mapping and prediction. Environmental Modelling and Software,

737 141(1), 105051. http://doi.org/10.1016/j.envsoft.2021.105051

738 Moore, I.D., Grayson, R.B., Ladson, A.R.: Digital terrain modelling: a review of

739 hydrological, geomorphological, and biological applications. Hydrological

740 Processes, 5(1), 3-30, 1991. https://doi.org/10.1002/hyp.3360050103

741 Ozgen-Xian, I., Kesserwani, G., Caviedes-Voullieme, D., Molins, S., Xu, Z.X.,

742 Dwivedi, D., Moulton, J.D., Steefel, C.I.: Wavelet-based local mesh refinement

743 for rainfall-runoff simulations. Journal of Hydroinformatics, 22(5), 1059-1077,

744 2020. https://doi.org/10.2166/hydro.2020.198

745 Rossman, L.A. Storm Water Management Model User's Manual Version 5.1;

746 EPA/600/R-14/413b; U.S. Environmental Protection Agency: Cincinnati, OH,

747 USA, 2015.

748 Schumann, G.J.P., Neal, J.C., Voisin, N., Andreadis, K.M., Pappenberger, F.,

749 Phanthuwongpakdee, N., Hall, A.C., Bates, P.D.: A first large-scale flood

750 inundation forecasting model. Water Resource Research 49(10):6248–6257, 2013.

751 https://doi.org/10.1002/wrcr.20521

752 Sánchez, R.R.: GIS-Based Upland Erosion Modeling, Geovisualization and Grid Size

753   Effects on Erosion Simulations with CASC2D-SED. Ph.D. Thesis, Colorado State

754   University, Fort Collins, CO, USA, 2002.

755 Singh J., Altinakar M.S., Yan D.: Two-dimensional numerical modeling of dam-break

756   flows over natural terrain using a central explicit scheme. Advances in Water

757   Resources,   34(10),   1366-1375,   2011.

758   https://doi.org/10.1016/j.advwatres.2011.07.007

759 Seyoum. S.D., Vojinovic, Z., Price, R.K., Weesakul, S.: Coupled 1D and noninertia 2D

760   flood inundation model for simulation of urban flooding. Journal of Hydraulic

761   Engineering   138(1):23–34,   2012.   https://doi.org/10.1061/(ASCE)HY.1943-

762   7900.0000485

763 Shen, Y., Jiang, C., Zhou, Q., Zhu, D., Zhang, D.: A Multigrid Dynamic Bidirectional

764   Coupled Surface Flow Routing Model for Flood Simulation. Water, 13, 3454,

765   2021. https://doi.org/10.3390/w13233454

766 Shen, Y., Jiang, C.: Quantitative assessment of computational efficiency of numerical

767   models for surface flow simulation. Journal of Hydroinformatics, 25 (3): 782–796,

768   2023. https://doi.org/10.2166/hydro.2023.131

769 Tarboton, D.G.: A new method for the determination of flow directions and upslope

770   areas in grid digital elevation models. Water Resources Research, 33(2), 662-670,

771   1997. https://doi.org/10.1029/96WR03137

772 Toro, E.F.: Shock-Capturing Methods for Free-Surface Shallow Flows. John Wiley,

773   2001.

774 Thompson, J.R., SoRenson, H.R., Gavin, H., Refsgaard, A.: Application of the coupled

775   MIKE SHE/MIKE 11 modelling system to a lowland wet grassland in southeast

776   England.   Journal   of   Hydrology,   293(1-4):   151-179.   2004.

777   http://doi.org/10.1016/j.jhydrol.2004.01.017

778   US Army Corps of Engineers, HEC-RAS User's Manual (version 6.4), 2023.

779   Van Leer, B.: Towards the ultimate conservative difference scheme V: A second order

780   sequel to Godunov's method. Journal of Computational Physics, 32(1), 101-136,

781   1979. https://doi.org/10.1016/0021-9991(79)90145-1

782   Wing, O., Sampson, C.C., Bates, P.D., Quinn, N., Neal, J.C.: A flood inundation

783   forecast of hurricane Harvey using a continental-scale 2D hydrodynamic model.

784   Journal   of   Hydrology   X,   4,   100039,   2019.

785   https://doi.org/10.1016/j.hydroa.2019.100039

786   Yu, W.: Research on Coupling Model of Hydrological and Hydraulics Based on

787   Adaptive Grid. Ph.D. Thesis, Tsinghua University, Beijing, China, 2019.

788   Xia, X., Liang, Q, Ming, X.: A full-scale fluvial flood modelling framework based on

789   a high-performance integrated hydrodynamic modelling system (HiPIMS).

790   Advances   in   Water   Resources,   132,   103392,   2019.

791   https://doi.org/10.1016/j.advwatres.2019.103392